Atmospheric
Chemistry
and Physics

Open Access

Global distributions, time series and error characterization of atmospheric ammonia (NH$_3$) from IASI satellite observations

M. Van Damme[1,2]**, L. Clarisse**[1]**, C. L. Heald**[3]**, D. Hurtmans**[1]**, Y. Ngadi**[1]**, C. Clerbaux**[1,4]**, A. J. Dolman**[2]**, J. W. Erisman**[2,5]**, and P. F. Coheur**[1]

[1]Spectroscopie de l'atmosphère, Chimie Quantique et Photophysique, Université Libre de Bruxelles, Brussels, Belgium
[2]Cluster Earth and Climate, Department of Earth Sciences, Vrije Universiteit Amsterdam, Amsterdam, the Netherlands
[3]Department of Civil and Environmental Engineering and Department of Earth, Atmospheric and Planetary Sciences, MIT, Cambridge, MA, USA
[4]UPMC Univ. Paris 06; Université Versailles St.-Quentin; CNRS/INSU, LATMOS-IPSL, Paris, France
[5]Louis Bolk Institute, Driebergen, the Netherlands

Correspondence to: M. Van Damme (martin.van.damme@ulb.ac.be)

Abstract. Ammonia (NH$_3$) emissions in the atmosphere have increased substantially over the past decades, largely because of intensive livestock production and use of fertilizers. As a short-lived species, NH$_3$ is highly variable in the atmosphere and its concentration is generally small, except near local sources. While ground-based measurements are possible, they are challenging and sparse. Advanced infrared sounders in orbit have recently demonstrated their capability to measure NH$_3$, offering a new tool to refine global and regional budgets. In this paper we describe an improved retrieval scheme of NH$_3$ total columns from the measurements of the Infrared Atmospheric Sounding Interferometer (IASI). It exploits the hyperspectral character of this instrument by using an extended spectral range (800–1200 cm^{-1}) where NH$_3$ is optically active. This scheme consists of the calculation of a dimensionless spectral index from the IASI level1C radiances, which is subsequently converted to a total NH$_3$ column using look-up tables built from forward radiative transfer model simulations. We show how to retrieve the NH$_3$ total columns from IASI quasi-globally and twice daily above both land and sea without large computational resources and with an improved detection limit. The retrieval also includes error characterization of the retrieved columns. Five years of IASI measurements (1 November 2007 to 31 October 2012) have been processed to acquire the first global and multiple-year data set of NH$_3$ total columns, which are evaluated and compared to similar products from other retrieval methods. Spatial distributions from the five years data set are provided and analyzed at global and regional scales. In particular, we show the ability of this method to identify smaller emission sources than those previously reported, as well as transport patterns over the ocean. The five-year time series is further examined in terms of seasonality and interannual variability (in particular as a function of fire activity) separately for the Northern and Southern Hemispheres.

1 Introduction

Human activities over the last decades have substantially perturbed the natural nitrogen cycle up to a level that is believed to be beyond the safe operating space for humanity (Galloway et al., 2008; Rockström et al., 2009, and references therein). Similar to the carbon cycle, anthropogenic perturbations to the nitrogen cycle originate from the production of energy and food to sustain human populations, which causes the release of reactive nitrogen compounds (collectively abbreviated as Nr), principally in the form of nitrogen oxides (NO$_x$ = NO + NO$_2$), nitrous oxide (N$_2$O), nitrate (NO$_3$) and ammonia (NH$_3$).

The Nr released into the environment is dispersed by hydrologic and atmospheric transport processes and can accumulate locally in soils, vegetation, and groundwater (Galloway et al., 2008). Excess Nr has important impacts on the environment, climate, and human health (e.g., Sutton et al., 2011; Erisman et al., 2013) such as loss of biodiversity, vegetation damage, and an increasing number of coastal dead zones (Bobbink et al., 2010; Krupa, 2003; Diaz and Rosenberg, 2011). In fact, one single nitrogen atom, moving along its biogeochemical pathway in ecosystems, can have a multitude of negative impacts in sequence (Galloway et al., 2003). This sequential process, known as the "nitrogen cascade", has been described in theory but quantitatively large uncertainties exist on atmospheric emissions as well as chemistry, transport, and deposition of Nr. These are such that our understanding of the environmental impacts of Nr is largely incomplete (Galloway et al., 2003; Erisman et al., 2013). It is commonly acknowledged that the major uncertainties are related to reduced nitrogen compounds, and in particular NH₃ (e.g., Sutton et al., 2011; Erisman et al., 2007; Fowler et al., 2013).

Globally, the EDGAR v4.2 emission inventory estimates that about 49.3 Tg of NH₃ was emitted in the atmosphere in 2008, with 81 % of this amount related to agriculture: 58 % to agricultural soils, 21 % to manure management, and 2 % to agricultural burning. The second most important source of NH₃ is vegetation fires (16 % of global emissions in 2008), with substantial year-to-year variability (EDGAR-Emission Database for Global Atmospheric Research, 2011). In addition, the relative importance of emission sources show large variations at local and regional scales: for instance, combustion associated with catalytic converters could contribute up to 10 % of the yearly emissions in the United States (Reis et al., 2009); in Europe the agricultural sector accounts for around 94 % of the NH₃ emissions (EEA-European Environment Agency, 2012).

In the atmosphere, NH₃ is a highly reactive and soluble alkaline gas. Reactions with acidic gases formed from NO_x, sulphur dioxide (SO2) emissions, as well as hydrochloric acid (HCl), can form secondary ammonium (NH_4^+) particles, which are important components of atmospheric aerosols of anthropogenic origin (Seinfeld, 1986; Pinder et al., 2008). In this respect, model studies have shown that a reduction of secondary particulate matter in Europe could only be effectively achieved by reducing NH₃ emissions in concert with the reduction of other primary gases (Erisman and Schaap, 2004). The large uncertainties in emissions combined with the complexity associated with modeling aerosol formation are such that current models do not satisfactorily reproduce atmospheric measurements of NH₃. Current models exhibit a general tendency to underestimate the concentrations, at least in the industrialized Northern Hemisphere (Heald et al., 2012).

Observing the spatial and temporal distribution of atmospheric NH₃ is therefore essential to better quantify emissions, atmospheric concentrations, and deposition rates and to develop and evaluate relevant management strategies for the future. Until recently, all available measurements were limited to surface sites (Erisman et al., 2007), providing only a local snapshot. Furthermore, these surface automated measuring devices are expensive and not always reliable, putting a limit on what can be expected from these in situ measurements (Erisman et al., 2003; Laj et al., 2009). It is worth noting that airborne (e.g., Nowak et al., 2007, 2010) as well as ship (e.g., Norman and Leck, 2005; Sharma et al., 2012) NH₃ observations have recently been reported but these are restrained to campaigns with limited temporal and spatial coverage. The recently discovered capability of advanced IR-sounders to probe atmospheric NH₃ (Beer et al., 2008; Coheur et al., 2009; Clarisse et al., 2009, 2010; Shephard et al., 2011) is an important step towards addressing this observational gap. In particular, the Infrared Atmospheric Sounding Interferometer (IASI), which is aboard the European MetOp polar orbiting satellites, offers the potential for monitoring NH₃ distributions globally and on a daily basis. This capability stems, on the one hand, from its scanning mode and, on the other hand, from its unprecedented hyperspectral and radiometric specifications. The first global distributions were acquired by IASI in 2009 following a simplified retrieval method (Clarisse et al., 2009) and by averaging the retrieved columns over a full year. In a subsequent case study of the San Joaquin Valley in California (Clarisse et al., 2010), a better understanding was achieved of what can be done with space-based measurements, and of the different parameters that affect measurement sensitivity (especially skin and atmospheric temperatures). It is shown that, when the detection is possible, the peak sensitivity for NH₃ is in the atmospheric boundary layer (Clarisse et al., 2010). Walker et al. (2011) introduced an innovative detection method, which substantially improves the NH₃ detection sensitivity of IASI. The availability of the satellite NH₃ measurements from IASI or the Tropospheric Emission Spectrometer (TES) has triggered work on particulate inorganic nitrogen in the United States: Heald et al. (2012) and Walker et al. (2012) used for this purpose one complete year of IASI measurements and a series of TES measurements, respectively, in combination with the GEOS-Chem model. Following these studies, TES measurements have been used to constrain emissions over over the United States (US) and have highlighted the underestimation of emission inventories, particularly in the west (Zhu et al., 2013). IASI measurements have also been used to confirm the importance of agricultural sources of anthropogenic dust and the non-negligible role of NH₃ in determining their properties (e.g., lifetime) (Ginoux et al., 2012). Finally, IASI-NH₃ observations over Asia have been compared qualitatively to GEOS-Chem NH₃ columns in Kharol et al. (2013), suggesting that the emissions in the model are not overestimated.

The present paper describes an improved retrieval scheme for near real-time global NH₃ retrievals from IASI, building

on the work of Walker et al. (2011). Here we retrieve NH$_3$ total columns from IASI with better sensitivity on a single measurement and on a twice-daily basis (i.e., using both the nighttime and daytime measurements); importantly, we also provide an appropriate error characterization. In the next section, we first review some of the main characteristics of IASI. In Sect. 3, the retrieval method is thoroughly described and its advantages are discussed against other existing retrieval schemes, especially the Fast Optimal Retrieval on Layers for IASI (FORLI) (Hurtmans et al., 2012). Section 4 provides an analysis of the global distributions of NH$_3$ acquired with this new retrieval method, underlining the improved sensitivity by the identification of new hotspots. In this last section the trends in NH$_3$ concentrations over five years of IASI operation are presented and discussed.

2 The Infrared Atmospheric Sounding Interferometer (IASI)

IASI is an infrared Fourier transform spectrometer, the first of which was launched aboard MetOp-A in October 2006 and has been operating since with remarkable stability (Hilton et al., 2012). A second instrument has been in operation on MetOp-B since September 2012, but here only the IASI-A measurements are analyzed. IASI combines the heritage of weather forecasting instruments with that of tropospheric sounders dedicated to atmospheric chemistry and climate (Clerbaux et al., 2009; Hilton et al., 2012). It circles in a polar Sun-synchronous orbit and operates in a nadir-viewing mode with overpass times at 9:30 local solar time (hereafter referred to as daytime measurements) and 21:30 local solar time (nighttime measurements) when it crosses over the Equator. The nadir views are complemented by measurements off-nadir along a 2100 km wide swath perpendicular to the flight line. With a total of 120 views along the swath, IASI provides near global coverage two times a day. It has a square field of view composed of four circular footprints of 12 km each at nadir, distorted to ellipse-shaped pixels off-nadir. IASI measures the infrared radiation emitted by the Earth's surface and the atmosphere in the 645–2760 cm^{-1} spectral range at a medium spectral resolution of 0.5 cm^{-1} apodized and low noise (~ 0.2 K at 950 cm^{-1} and 280 K) (Clerbaux et al., 2009). The spectral performance and high spatial and temporal sampling makes IASI a powerful sounder to monitor atmospheric composition, with routine measurements of greenhouse gases and some reactive species (in particular CO, O$_3$, HNO$_3$) and other short-lived species, including NH$_3$, above source regions or in very concentrated pollution plumes. In total, 24 atmospheric species have been identified in the IASI spectra (Clarisse et al., 2011).
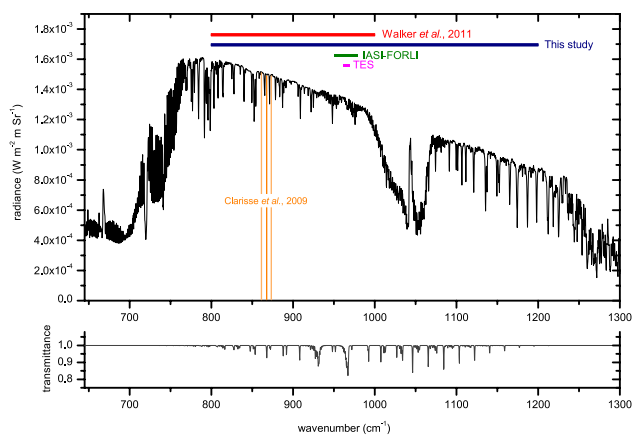

Fig. 1. Top: Example of an IASI spectra between 645 and 1300 cm^{-1} measured on 30 August 2011 in the California San Joaquin Valley (USA). The orange range was used for the first global NH$_3$ distribution obtained by satellite (Clarisse et al., 2009), with the vertical lines representing the channels used to compute the brightness temperature difference. The green range shows the spectral interval used by FORLI on IASI spectra and the pink ranges the microwindows used for TES NH$_3$ retrievals (Shephard et al., 2011). The large red and dark blue ranges are the continuous spectral intervals used for the NH$_3$ detection in Walker et al. (2011) and in this work, respectively. Bottom: Transmittance of ν_2 vibrational band of NH$_3$.

3 Retrievals of NH$_3$ from IASI

3.1 Overview of retrieval schemes and spectral ranges

NH$_3$ is detected in the thermal infrared spectral range in its ν_2 vibrational band centered at around 950 cm^{-1} (Beer et al., 2008; Coheur et al., 2009). While many spectral features are potentially usable in the spectral range between 750 and 1250 cm^{-1} (Fig. 1), the early retrievals from TES and IASI have only used part of the available spectral information. For instance, TES retrievals (Shephard et al., 2011), which are based on an optimal estimation strategy and provide weakly-resolved profiles, exploit only a set of microwindows within the strong Q-branch between 960 and 970 cm^{-1} (pink ranges in Fig. 1), while the first global distributions from IASI were acquired using a brightness temperature difference based on a single NH$_3$ feature at 867.75 cm^{-1} (vertical orange lines in Fig. 1) (Clarisse et al., 2009). Near real-time distributions of NH$_3$ were later obtained from the Fast Optimal Retrieval on Layers for IASI (FORLI) processing chain described elsewhere in detail for CO, O$_3$, and HNO$_3$ profiles (Hurtmans et al., 2012). FORLI relies on a full radiative transfer model using the optimal estimation method for the inverse scheme. For the NH$_3$ profile retrievals it uses specifically a priori constraints from the TM5 model and a spectral range from 950 to 979 cm^{-1} (green range in Fig. 1). FORLI retrievals are, however, only performed on the IASI spectra from the morning orbit and for which the NH$_3$ signal is clearly detected
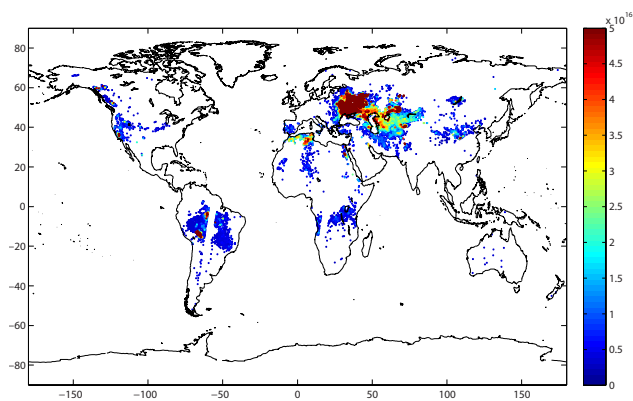
Fig. 2. IASI morning NH$_3$ observations (molec cm^{-2}) on 15 August 2010 obtained using the FORLI processing chain. The high concentrations measured in eastern Europe are due to the exceptional emissions from the large Russian fires in the summer of 2010 (R'Honi et al., 2013).

in a first step. This produces a limited number of retrievals per day, which favor high concentrations (an example is provided in Fig. 2). Preliminary usage of the FORLI-NH$_3$ retrieved profiles for model studies also revealed difficulties in using the averaging kernels (Heald et al., 2012), which are too low and not representative of the available information in the measurements as a consequence of the retrieval settings chosen to ensure stability and convergence with the optimal estimation framework.

The retrieval scheme we developed here avoids these weaknesses. One element of our improved retrieval algorithm relies on the detection algorithm of Walker et al. (2011), which allows using a large spectral range. In fact, we extend the 800–1000 cm^{-1} range (red range in Fig. 1) used in Walker et al. (2011) to 800–1200 cm^{-1} (dark blue range in Fig. 1). The second element of our improved algorithm is akin to the brightness temperature differences to column conversion from Clarisse et al. (2009), but also accounting for the NH$_3$ spectral signature dependence on thermal contrast.

3.2 A retrieval scheme based on the calculations of hyperspectral range index

The retrieval scheme presented here is built on the detection method described by Walker et al. (2011), which can detect trace gases better than any other known method. It works especially well for those species which are only sometimes seen in IASI spectra. The first step is an extension of this detection method and consists of calculating a so-called Hyperspectral Range Index (HRI hereafter) from each IASI observation; in the second step the HRI is converted into a NH$_3$ total column using large look-up tables built from forward radiative transfer calculations under various atmospheric conditions. The two steps are detailed below.

3.2.1 Hyperspectral Range Index (HRI)

As opposed to brightness temperature differences (ΔBT) which usually rely on a single specific spectral channel in which the target species is optically active, the HRI takes into account a broad spectral range to increase sensitivity. For NH$_3$ from IASI we consider almost the entire ν_2 vibrational band, from 800 to 1200 cm^{-1} (dark blue range in Fig. 1). The method developed in Walker et al. (2011) relies on the optimal estimation formalism (Rodgers, 2000), but with a generalized noise covariance matrix that contains the entire expected spectral variability due to all atmospheric parameters except NH$_3$, in addition to the usual instrumental noise. In the spectral range selected here, the variability is associated mainly with temperature, ozone, water, clouds, and surface emissivity. In addition to lowering the detection threshold, the method has the advantage of providing in a single retrieval step (assuming linearity of the NH$_3$ signature around a vanishingly small abundance) a quantity that is representative of the NH$_3$ abundance, without having to retrieve other parameters. It is this quantity that we refer to as the HRI. It is similar, other than units, to the apparent column retrieved in Walker et al. (2011). However, unlike the optimal estimation method, no information about the vertical sensitivity can be extracted. The use of a fixed Jacobian to calculate HRI does not allow generating meaningful averaging kernels.

More specifically, we first construct a mean background spectrum $\bar{\mathbf{y}}$ and associated variance-covariance matrix $\mathbf{S}_y^{\text{obs}}$ from spectra that are assumed to have no detectable NH$_3$ signature. With these the HRI of a measured spectrum $\mathbf{y}$ is defined as

$$\text{HRI} = \mathbf{G}(\mathbf{y} - \bar{\mathbf{y}}) \tag{1}$$

with $\mathbf{G}$ the measurement contribution function

$$\mathbf{G} = \left(\mathbf{K}^T \mathbf{S}_y^{\text{obs}-1} \mathbf{K}\right)^{-1} \mathbf{K}^T \mathbf{S}_y^{\text{obs}-1}. \tag{2}$$

Here $\mathbf{K}$ is the difference between a spectrum simulated with a given (small) amount and a spectrum simulated without NH$_3$. For the forward model the Atmosphit software was used (Coheur et al., 2005). With these definitions, $\mathbf{K}$ and $\mathbf{G}$ have respectively radiance and inverse radiance units. The HRI is, as a matter of consequence, dimensionless and will be either positive or negative, depending on the sign of $\mathbf{K}$ (positive for an absorption spectrum and negative for an emission spectrum).

For the calculation of $\bar{\mathbf{y}}$ and $\mathbf{S}_y^{\text{obs}}$ we used a subset of the IASI spectra measured on the 15 August 2010 (around 640 000 spectra in total), in which no NH$_3$ was detected. To select spectra with no detectable ammonia signature, we used an iterative approach (Clarisse et al., 2013). First, all spectra showing a significant brightness temperature difference at 867.75 cm^{-1} (ΔBT > 0.25 K) were excluded (Clarisse et al., 2009). Second, from the remaining set, an initial variance–covariance matrix $\mathbf{S}_y^{\text{obs}}$ was built using the spectral interval
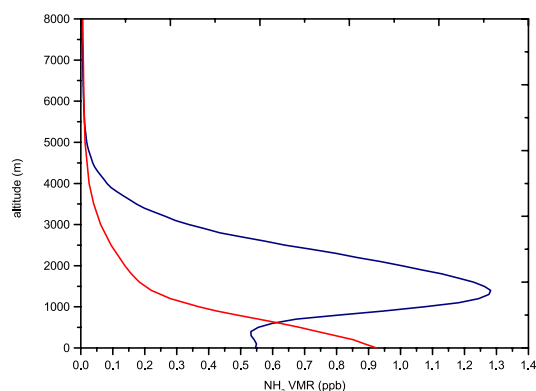
Fig. 3. NH$_3$ GEOS-Chem model profiles above a source area (red) and transported above sea (blue), used as reference for the radiative transfer simulations.

Fig. 4. Look-up tables used to convert HRI into NH$_3$ total columns through the thermal contrast (left panels) with the associated retrieval error (right panels), above land (top panels) and sea (bottom panels). The tables are built from about 450 000 simulated IASI spectra above land and about 116 000 above sea; see text for details.

between 900 and 970 cm^{-1} and the HRI initially calculated. Finally, the spectra with a measurable HRI were removed to build a new S_y^{obs} between 800 and 1200 cm^{-1}, which ultimately includes around 500 000 NH$_3$-free measurements.

The conversion of the HRI to total columns of NH$_3$ is not straightforward and requires full radiative transfer simulations. In our method, the conversion is done using theoretical look-up tables (LUTs) to achieve fast processing of the IASI data set from 2007 to the present.

3.2.2 Look-up tables

The LUTs were built by simulating a large amount of IASI spectra using a climatology of 4940 thermodynamic atmospheric profiles above land and 8904 profiles above sea (Chevallier, 2001) with the Atmosphit line-by-line radiative transfer model. For these two categories a reference NH$_3$ vertical profile was used (Fig. 3), which was constructed from a series of GEOS-Chem (www.geos-chem.org) v8.03.01 model profiles representative of polluted (for the land) and transported (for the sea) conditions in 2009 at 2° × 2.5° horizontal resolution. Model simulations were used as a substitute for representative NH$_3$ measured profiles that were not available. Figure 3 shows that the land standard profile peaks at the surface and decreases rapidly with altitude, whereas the ocean profile has its maximum at around 1.4 km. To include in the LUTs a representative set of NH$_3$ concentrations, the profiles were scaled by 13 different values from 0 to 10 (0; 0.1; 0.3; 0.5; 1; 1.5; 2.0; 3.0; 4.0; 5.0; 6.5; 8.0; 10.0) for the ocean and by 30 different values from 0 to 200 (0; 0.1; 0.3; 0.5; 1.0; 1.5; 2.0; 2.5; 3.0; 4.0; 5.0; 6.5; 8.0; 10; 12.5; 15; 20; 25; 30; 35; 42.5; 50; 62.5; 75; 87.5; 100; 125; 150; 175; 200) for the land. The largest concentrations for the simulations thus correspond to a concentration at the surface of close to 185 ppb.

In addition to the varying NH$_3$ concentrations, a critical dimension in the LUTs is the thermal contrast near the sur-
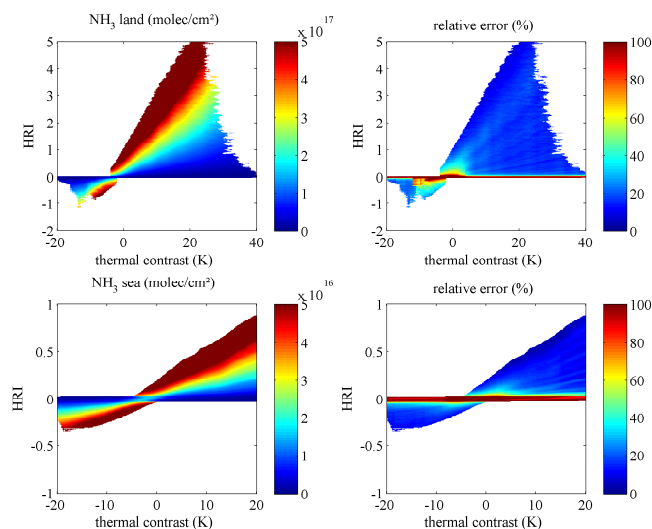
face, which drives the sensitivity of the infrared measurements to boundary layer concentrations (e.g., Clarisse et al., 2010; Bauduin et al., 2014; Deeter et al., 2007). It is defined here as the difference between the skin (surface) temperature and that of the air at an altitude of 1.5 km. While the climatology of Chevallier (2001) encompasses a range of thermal contrasts, it does not include enough variability for the large values that are the most favorable for probing NH$_3$ (Clarisse et al., 2010). To ensure that the LUT characterizes these larger thermal contrasts, the surface temperature was artificially changed for each of the atmospheric profiles to provide reference cases characterized by thermal contrasts up to −20 to +20 K for the sea and −20 to +40 K for the land.

With these inputs, around 450 000 and 116 000 IASI spectra were simulated for land and sea, respectively, from which theoretical HRI values were calculated following Eq. (1). The LUTs, calculated independently for land and sea, link the HRI to the NH$_3$ column concentration (in molec cm^{-2}) and thermal contrast (K). This is achieved by averaging all the NH$_3$ columns in a box determined by a given thermal contrast and a given HRI plus/minus as an estimated error on each. The error on the thermal contrast (TC) is taken as $\sqrt{2} \times 1$ K (considering that both the skin and air temperature have an uncertainty of about 1 K; Pougatchev et al., 2009) while the error on the HRI was taken as 0.0306, which corresponds to the standard deviation of HRI calculated for spectra above an area without NH$_3$ (20–30° N 30–40° W) for a period of 6 days (1–3 May 2010 and 1–3 October 2010). The resulting LUTs are depicted in Fig. 4. It shows that a given HRI can be associated with different values of the NH$_3$ column, depending on thermal contrast: for values of thermal

contrasts close to zero the HRI is almost vanishing (indicating a signal below the measurement noise) and basically all values of NH₃ total columns are possible for a narrow HRI range. In contrast, for the largest values of TC, there is a one-to-one correspondence between HRI and the NH₃ column. This dependence also appears very clearly in the estimated errors (right panels in Fig. 4) which are calculated as the standard deviation of the NH₃ columns inside the box defined previously. Errors are the largest (above 100 %) for low values of TC and/or HRI, but above land they are generally well below 25 % for TC above a few K and HRI larger than 0.5. Above sea, the HRI does not include large values (because the concentration range included in the forward simulations is smaller) but the relative errors follow the same behavior.

As the LUTs were built for a zero viewing angle, a cosine factor was applied to the calculated HRI values before the conversion in the LUTs to account for the increased path length at larger angles. The cosine factor was verified to properly correct the angle dependence for larger values of HRI. However, for lower values and low thermal contrasts, this factor appears to overcorrect and introduces a low bias for the larger angles. This is possibly caused by the fact that the noise error covariance matrix partially accounts for the viewing angle when the spectral noise dominates over the NH₃ spectral signature. In future versions of this product, the angle dependence could be removed completely by the use of angle dependent error covariance matrices.

A last source of error arises from the retrieval sensitivity to the vertical distribution of NH₃. This sensitivity is not included in the error assessment presented here as the measurements provide no information regarding the NH₃ vertical profile. As previously explained, two fixed profiles were chosen to retrieve NH₃ columns: a source profile for land and a transported profile for sea. Such an approach allows us to provide a coherent five-year data set produced with reasonable computational power. To test the dependence of the retrieval on the vertical profile used to build the LUTs, we have taken the observations over land on 15 August 2010 and used the LUT made for sea observations – built with a transported profile – to retrieve the concentrations. We compare the two sets of retrieved values and find that a regression line weighted by the error on the retrievals suggests a factor of two between the NH₃ columns obtained from a profile having its maximum at the surface and the columns obtain from one having its maximum at 1.4 km. Given that the two profiles differ substantially, it is reasonable to conclude that in the large majority of cases the factor of two is likely an upper bound for the error introduced by considering these constant NH₃ land/sea profiles.

Considering a detection threshold defined as 2σ on the HRI, an indicative total column detection threshold of NH₃ as a function of thermal contrast can be calculated using the LUTs. The result is shown in Fig. 5 separately for land (red curve) and for sea (blue curve). It indicates that when the contrast in temperature is low (a value of -2.9 K for TC
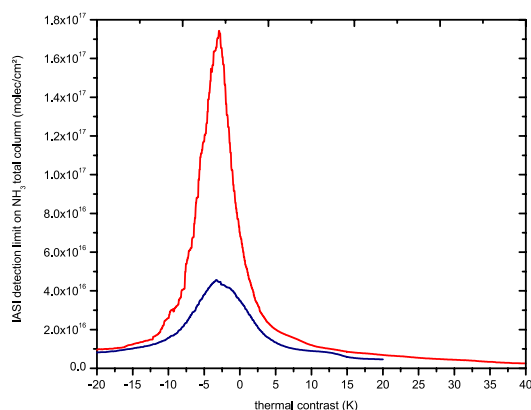

Fig. 5. Lowest possible detectable NH₃ total column, in molec cm⁻², above land (red) and sea (blue). The values are those for which the retrieved column would be significant below 2σ in HRI.

at 1.5 km corresponds to an almost vanishing contrast between the surface and the air just above it), the measurement is insensitive to even very high concentrations of NH₃. For the more favorable values of TC the IASI measurements should be able to measure NH₃ down to the 10^{16} molec cm⁻² level. As an illustration, this detection limit would allow measuring NH₃ columns year round in the San Joaquin Valley, where we measure columns varying above 10^{16} to 4.3×10^{17} molec cm⁻² for 81 % of the observations (median at 3.2×10^{16} molec cm⁻²).

3.2.3 Global processing of IASI data

The HRI are calculated following Eq. (1) from the IASI Level 1C radiance spectra, using the meteorological Level 2 information from the operational IASI processor (August et al., 2012) to calculate the thermal contrast. Note that occasionally the meteorological Level 2 data contain a complete temperature profile but no surface temperature. To not lose valuable data, for these scenes we retrieve the surface temperature directly from the spectra using window channels at 957 and 2143 cm⁻¹ (keeping the highest value) and the spectral emissivity database provided by Zhou et al. (2011). An example of processing is shown in Fig. 6 for the same day (15 August 2010, morning overpass time), as in Fig. 2. HRI distribution (top-left panel, Fig. 6) depicts a global coverage with highest values over eastern Europe and Russia associated with the large fires outside of Moscow in 2010. Thermal contrast (top-right panel, Fig. 6) is positive and high for low- and mid-latitudes and lower at higher latitudes; it is negative above Antarctica and part of Greenland. Data filtering is needed to remove unreliable columns from the NH₃ distribution. The bottom panel of Fig. 6 shows data only for the scenes that have a cloud fraction below 25 % and a surface temperature above 265.15 K. A more strict data filtering could be carried out by using the error (bottom-left
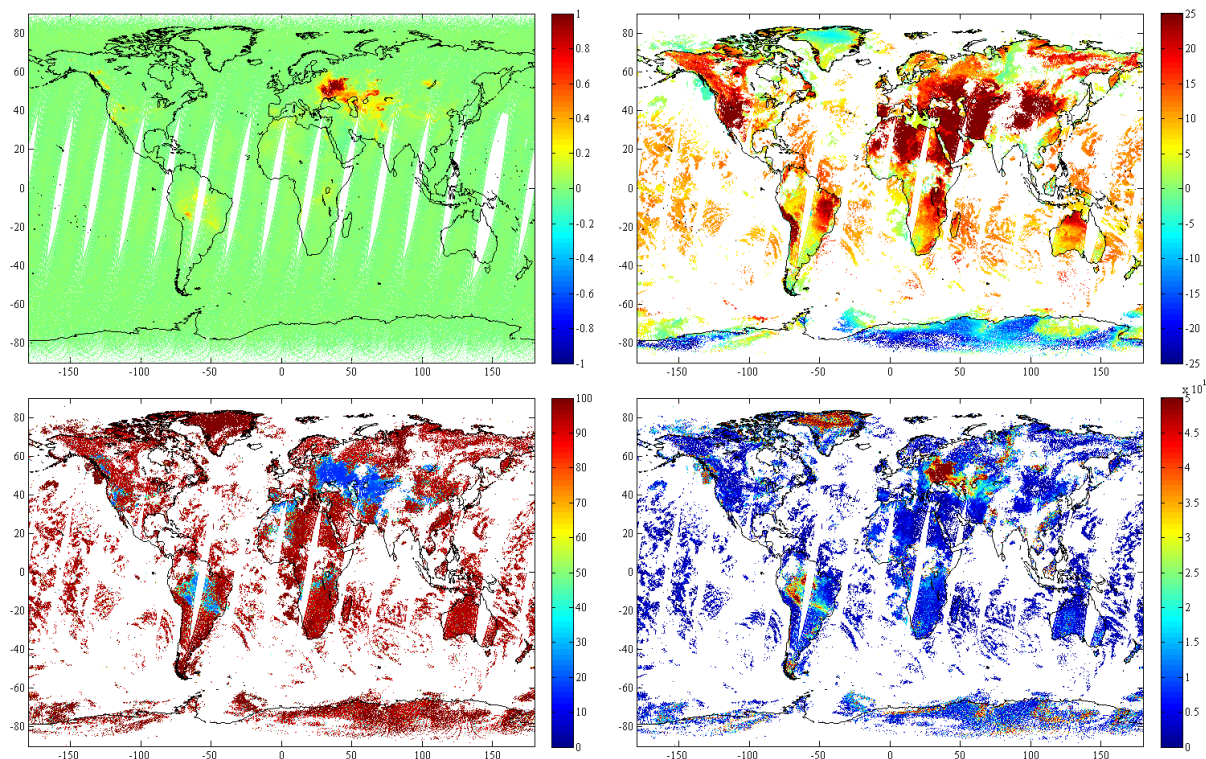
Fig. 6. From top to bottom and from left to right: HRI (no unit), thermal contrast (K), relative error (%) and NH$_3$ total columns (molec cm^{-2}) with posterior filtering, for 15 August 2010 in the morning, as in Fig. 2. The filtering applied here (apart from the HRI) removes all points with a cloud fraction above 25 % and a surface temperature below 263.15 K.

panel, Fig. 6) to exclude unreliable columns, including the high measurements observed above Greenland or Antarctica. The comparison between Figs. 2 (FORLI optimal estimation scheme) and 6 (our new HRI-based retrieval scheme) reveal a significant additional number of daily retrieved NH$_3$ column values. As an indication, even considering only values with an error below 50 %, we estimate a net gain of 16 082 measurements (or an additional 63 % number of measurements) with our improved scheme.

4   Results and discussion

4.1   Product evaluation

A first characterization of the product is provided in Fig. 7, with a histogram of the relative error on the retrieved NH$_3$ column for four different situations corresponding to land and sea observations, separately for the IASI morning and evening overpasses. The histogram, which is based on five years of observations, shows that the majority of measurements have an error above 75 %. These situations correspond to small values of the HRI (small NH$_3$ column and/or low value of the thermal contrast), and are, as expected, mainly above sea. Retrievals with an error smaller than 75 % are found above land and sea primarily during daytime (espe-

cially for the lowest errors), when the thermal contrast is generally positive. As will be shown in Sect. 4.2 (see for example Fig. 10), the NH$_3$ measurements above sea are all in coastal regions and can be attributed unambiguously to transport from nearby continental sources. Another important conclusion from Fig. 7 comes from the significant number of retrieved columns with errors below 50–75 % during the evening overpass of IASI, and which are very likely associated with temperature inversions at a given altitude within the boundary layer, i.e., negative thermal contrasts, which strongly increase the retrieval sensitivity at that altitude (Clarisse et al., 2010; Bauduin et al., 2014). Finally, we conclude that the retrievals with the lowest errors (smaller than 25 % on the column) are obtained above land for the daytime overpass and are associated with a large positive thermal contrast and a significant amount of NH$_3$.

To test the performance of the different detection methods and retrieval ranges we compare them in terms of sensitivity. As the different quantities (brightness temperature differences and effective retrieved columns) have different units, it is useful to look at the noise-to-signal ratio, which is dimensionless. As a measure of the signal we take the mean retrieved value of a collection of 100 spectra with a strong NH$_3$ signature. This value can then be used as a normalization factor for the noise. To measure the noise we take a large
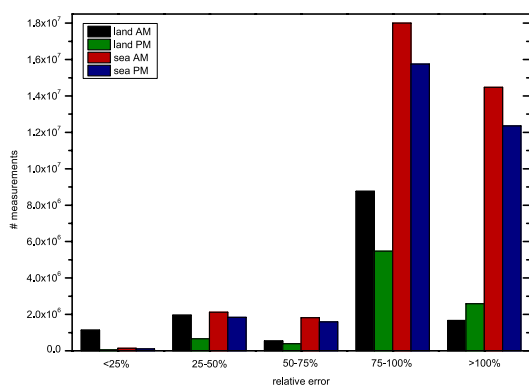
Fig. 7. Number of IASI NH$_3$ measurements with relative errors on the total column in the range 0–25, 25–50, 50–75, 75–100 and above 100 % over five years (from 1 November 2007 to 31 October 2012).

Fig. 8. Histogram of the Θ values of the new retrieval scheme (orange), for a smaller hyperspectral range (green) and for a brightness temperature difference detection method (Clarisse et al., 2009) (blue) for 15 August 2010 (morning overpass). The standard deviation (STD) of Θ values associated with each approach shows the gain of sensitivity of this work using the HRI-based retrieval scheme.

collection of spectra with no detectable NH$_3$ signature and for which we expect the retrieved (normalized) value (which we called Θ) to be close to zero. The distribution of Θ values for the different detection methods is depicted in Fig. 8. A good measure of the noise-to-signal ratio is the standard deviation of these distributions. Our newly developed scheme, based on the calculation of the HRI, provides the smallest standard deviation (0.04), indicating a gain of sensitivity as compared to the other detection methods. The comparison with an HRI calculation based on a smaller spectral range (800–1000 cm^{-1}, STD = 0.07) indicates the improvement given by the consideration of an extended range (800–1200 cm^{-1}). The improvement is largest in comparison to the initial brightness temperature approach presented in (Clarisse et al., 2009), characterized here by a standard deviation of 0.30.

A quantitative comparison between the NH$_3$ total columns retrieved from FORLI and the HRI scheme presented here is provided in Fig. 9. The comparison is shown separately for one day (15 August 2010 – similar to Figs. 2 and 6) and one year (2011, right panel) of IASI measurements, and is shown as a function of the HRI retrieval error (color bar). The agreement is excellent (closely matching the 1 : 1 slope) for the HRI retrievals with the smallest errors, as clearly seen for 15 August, a day with very large NH$_3$ total columns due to the fires in Russia. For the HRI derived columns with an error above 50 %, the FORLI retrievals are close to the a priori, indicative of a small NH$_3$ signature due to either low NH$_3$ or small values of the thermal contrast. When taken globally, the correlation between the columns retrieved by the two methods is high (Pearson's r coefficient of 0.81 for the year 2011) but with the HRI columns on average 35 % lower. Overall the agreement is very good, considering the very different approaches and the dependence of the FORLI retrievals on the a priori. The HRI-based retrieval scheme removes this dependence, allows retrieval for the daytime and
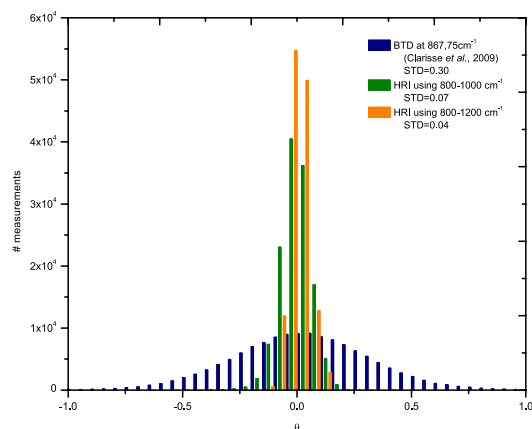
nighttime overpasses, above land and sea, and has the advantage of providing an associated error with each observation.

4.2 Global and regional distributions

With the HRI retrieval scheme, global distributions of NH$_3$ have been retrieved from IASI level 1C twice a day over five years of IASI measurements from 1 November 2007 to 31 October 2012. As the amount of daily data is not always sufficient to obtain meaningful global distributions (due to cloud cover and the availability of the temperature profiles from the EUMETSAT operational processing chain), it is convenient to consider monthly or yearly averages for some applications. However, averaging is not straightforward as the error is highly variable. To tackle this issue two approaches can be followed: applying a pre-filtering of the measurements by the relative error followed by an arithmetic averaging or using a weighted averaging method on the entire data set. The pre-filtering approach has the advantage of using only those measurements with the lowest error, but will lead naturally to a bias of the average towards the highest values (for which the error is lower). The weighted averaging method has the advantage of using all of the IASI observations and therefore introduces a smaller bias into the averaging. This is the approach chosen in what is presented next, where the measurements over the period of interest are further gridded in 0.25° × 0.5° cells. The column in each cell is then a weighted average:

$$\overline{x} = \frac{\sum w_i x_i}{\sum w_i}, \tag{3}$$

where $w_i = 1/\sigma^2$ and σ is the error – relative or absolute – on the retrieved column estimated on a pixel basis. The mean
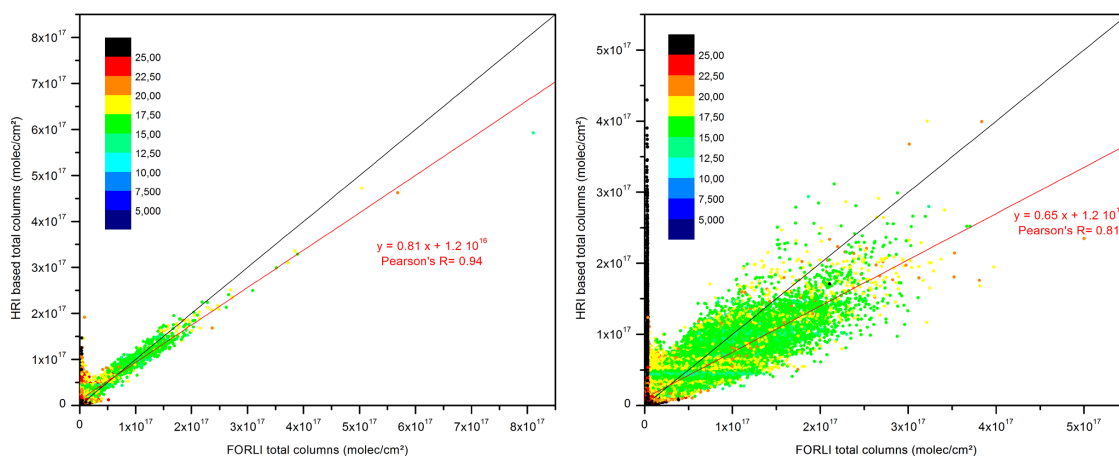
Fig. 9. NH$_3$ total columns in molec cm^{-2} retrieved in this work from the HRI retrieval scheme (y axis) versus those retrieved by FORLI (x axis) for 15 August 2010 (left panel) and over the entire year 2011 (right panel). The colors refer to the error calculated with the HRI retrieval scheme. The black line represents the 1 : 1 slope and the red line the linear regression weighted by the HRI retrieval errors. The Pearson's r coefficient, the values of slope and intercept from the linear regression are also given.

column itself can be assigned an error $\overline{\sigma}$, which is calculated in a similar way:

$$\overline{\sigma} = \frac{\sum \frac{1}{\sigma_i}}{\sum \frac{1}{\sigma_i^2}}. \tag{4}$$

Figure 10 shows the NH$_3$ total column distribution in molec cm^{-2} averaged using relative error weighting over the five years, separately for the morning (top panel) and evening (bottom panel) overpass time. Note that a post-filtering of the mean columns in the cells has also been carried out to obtain more reliable distributions: all cells with less than 50 (150) measurements per cell and a mean error $\overline{\sigma}$ larger than 75 % (58 %) for the morning orbit above land (sea) have been rejected. The same was done for the evening data, with threshold values of 100 (300) individual observations per cell and 100 % (58 %) on the mean error in the cell. Also the relative error weighted averaging approach using Eq. (3) preferentially accounts for measurements with low relative error and this explains the large impact of fires plumes, as the IASI sensitivity and the NH$_3$ retrieval scheme efficiency is higher in these cases. Conversely, weighting with the absolute value of the error may introduce a lower bias as large columns with low relative error can still have large errors in absolute terms. Distributions averaged using absolute errors for the weighting are shown in Fig. 11, similarly to Fig. 10. We have also carried out a post-filtering on the global distributions of Fig. 11: for the morning mean, we have excluded all pixels with less than 100 measurements and a mean absolute error larger than 90 % of the averaged column above land and sea; for the evening mean, we have excluded data with less than 100 measurements per cell for land and sea and with an absolute error larger than the averaged columns for land and than 90 % of the averaged columns for sea. The differences

between Figs. 10 and 11 highlight the challenges associated with averaging data with large variability in concentrations and errors. In the following discussion, we consider only the distributions weighted with relative errors as it is representative of the more reliable observations and highlights all the events where high columns are observed over the course of the five years.

The daytime distribution (top panel in Fig. 10) shows extreme average column values (up to 1.5×10^{17} molec cm^{-2} with error around 60 %) in Russia, which are due to the 2010 large fires and associated NH$_3$ emissions that persisted for several weeks in August 2010 (see R'Honi et al., 2013, and references therein). Other fire-related hotspot regions are seen over Alaska (from the 2009 fires), eastern Russia (2011), South America (mainly from 2010), and central Africa (throughout 2008–2012).

Most other hotspot regions are related to agriculture. Asia is responsible for the largest NH$_3$ emissions (EDGAR-Emission Database for Global Atmospheric Research, 2010), especially then over the Indo-Gangetic plain where we estimate total columns up to 6.4×10^{17} molec cm^{-2} (19 % error). This area is well known for its intensive agricultural practices and its industrial emissions (EDGAR-Emission Database for Global Atmospheric Research, 2011). Additional hotspot regions include the Fergana Valley and the central Asia area irrigated by the Syr Darya and the Amu Darya in Uzbekistan and Kazakhstan highlighted in previous studies (Scheer et al., 2008; Clarisse et al., 2009), as well as the North China Plain in China (see Fig. 13 and Clarisse et al., 2009). While many of these larger hotspots have already been identified in our previous study (Clarisse et al., 2009) our new retrieval scheme allows detection of smaller and weaker NH$_3$ sources. A striking example is the NH$_3$ detected above regions associated with the development of
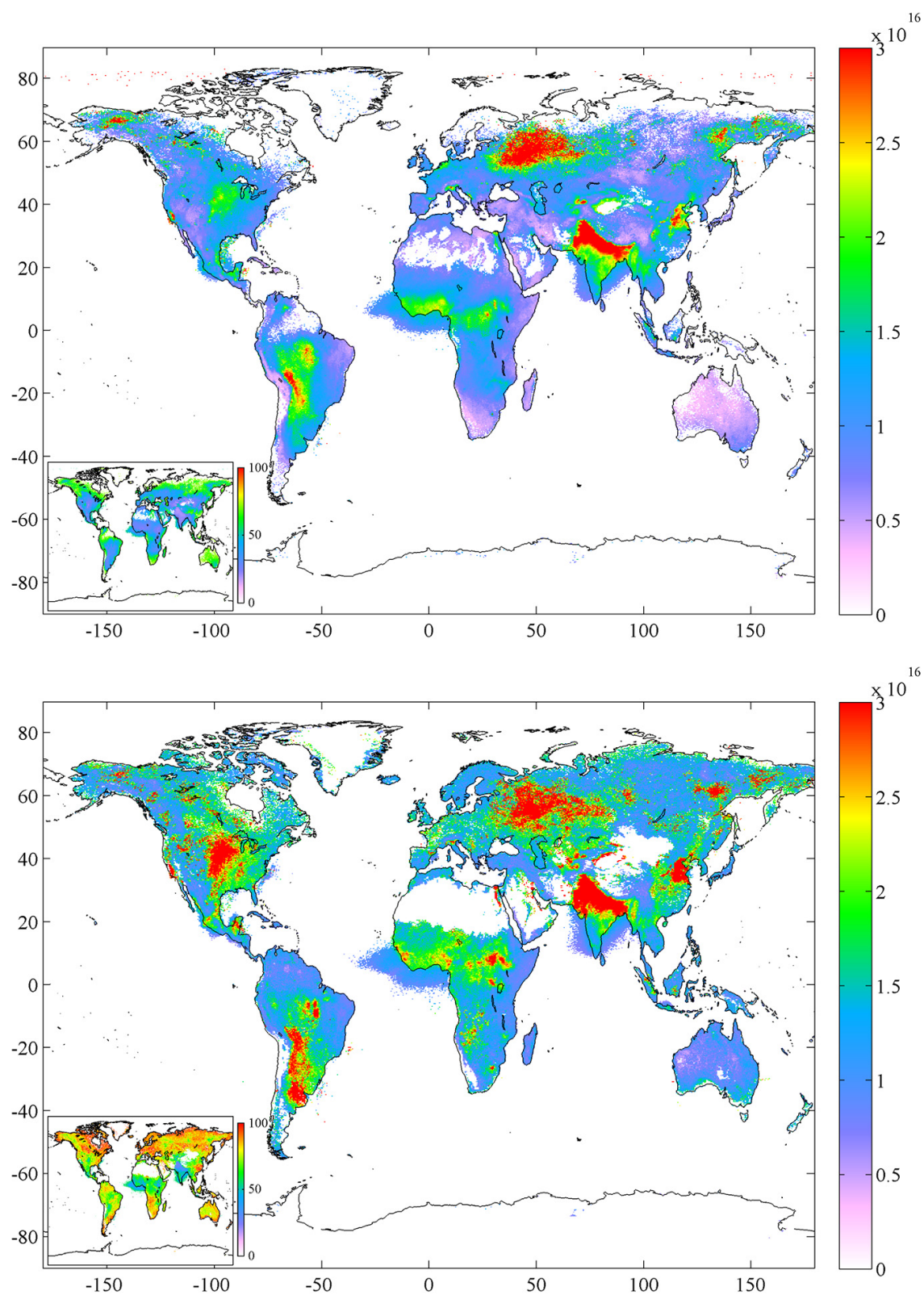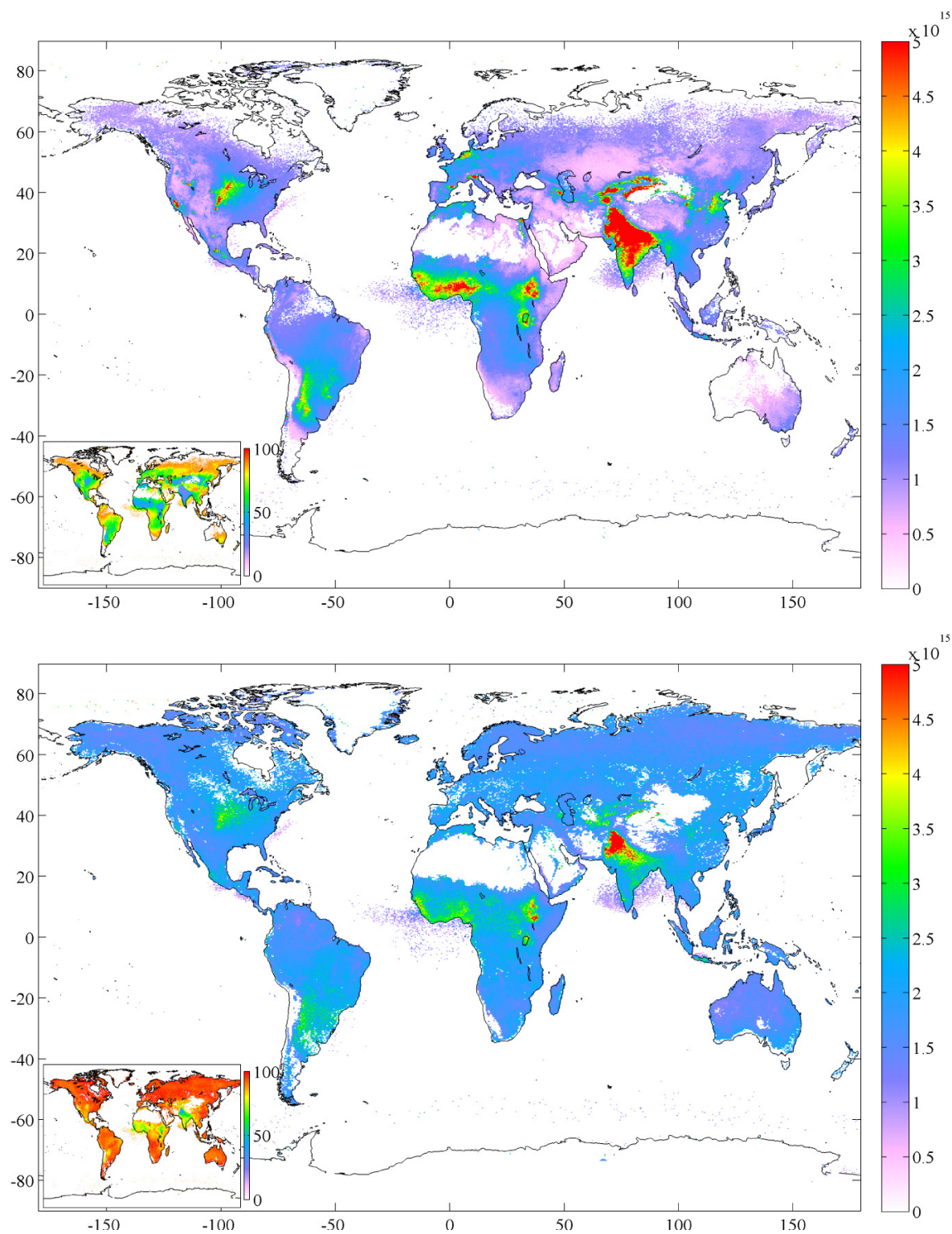
Fig. 10. NH$_3$ total columns (molec cm^{-2}) and relative error (bottom-left inset, %) distributions for five years of IASI measurements (1 November 2007 to 31 October 2012), in $0.25° \times 0.5°$ cells for the morning (top panel) and evening (bottom panel) overpasses. The NH$_3$ distributions are a mean of all measurements within a cell, weighted by the relative retrieval error following Eq. (3). The error distributions are a weighted mean of the relative error of all observations within a cell, following Eq. (4).

Fig. 11. NH$_3$ total columns (molec cm^{-2}) and relative error (bottom-left inset, %) distributions for five years of IASI measurements (1 November 2007 to 31 October 2012), in $0.25° \times 0.5°$ cells for the morning (top panel) and evening (bottom panel) overpasses. The NH$_3$ distributions are a mean of all measurements within a cell, weighted by the absolute retrieval error following Eq. (3). The error distributions are a weighted mean of the absolute error of all observations within a cell following Eq. (4) and divided by the NH$_3$ total columns to provide an error distribution in %.
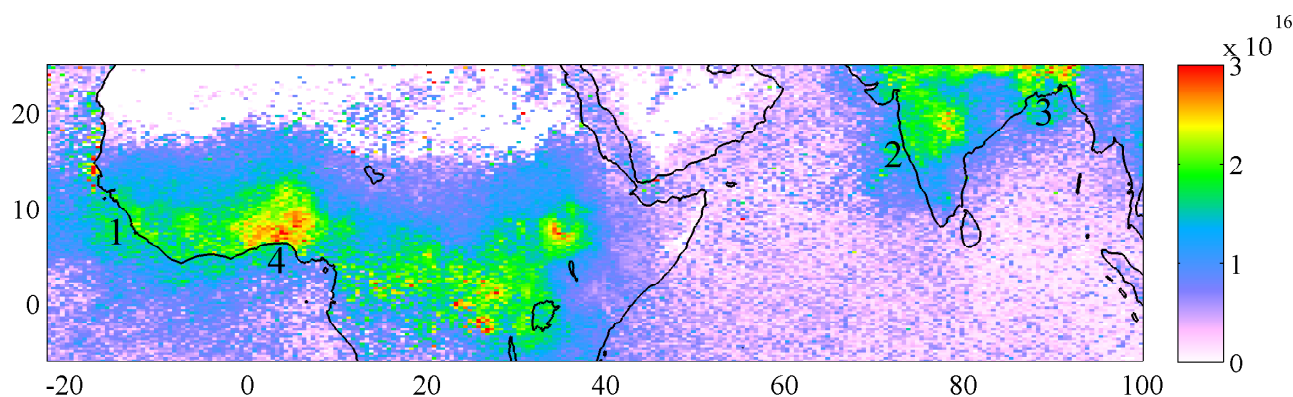
Fig. 12. NH$_3$ total columns (molec cm^{-2}) distribution averaged for February 2011. A post-filtering has been carried out excluding columns with a mean error above 100 %. Transported NH$_3$ is observed mainly from fire plumes on the west and south coast of western Africa (1), and mainly from agricultural sources on the west coast of India (2), the Bay of Bengal (3) and the Gulf of Guinea (4).

intensive center-pivot irrigation agriculture in Saudi Arabia already seen by the LANDSAT instrument (NASA, 2012). Other newly identified source areas in Asia include the mouth of the Shatt al-Arab river (Iraq), Thailand and Indonesia. These are likely caused by biomass burning events on the Borneo and Sumatra Islands (Justice et al., 2011) and intensive fertilizer application on Java Island (Potter et al., 2010).

The distribution of atmospheric NH$_3$ in South America is driven by the fire events in 2010 (e.g., center of Brazil), but we can also identify new agricultural hotspots around Santiago (Chile) and in the Llanos area (Columbia, Venezuela) (LADA, 2008; Potter et al., 2010). Two main agricultural source areas show up in North America: the US Midwest region and the San Joaquin Valley (California, US), where high NH$_3$ columns are observed throughout the year (Clarisse et al., 2010) and up to 6.0×10^{16} molec cm^{-2} (17 % error). NH$_3$ columns are also now retrieved above eastern states of the US. Other new source areas are identified in Canada, for example southeast of Calgary and southeast of Winnipeg. Both areas are known for their high anthropogenic NH$_3$ emission (Environment Canada, 2013). In Africa, the largest columns are found over major agricultural regions, especially western Africa (Adon et al., 2010) as well as Sudan and Ethiopia (LADA, 2008). The largest columns were found in Nigeria, where averaged columns up to 2.6×10^{16} molec cm^{-2} (39 % error) were measured. Previously unreported hotspots include the Zambezi basin (Mozambique) and particularly the Bethal/Secunda area (South Africa). The location of the latter suggests industrial emissions as the main source. The availability of retrievals over Oceania highlights hotspots in southern Australia and New Zealand, which correspond to the main agricultural land use systems for this continent (LADA, 2008; Potter et al., 2010). In Europe, the highest values are measured above the Italian Po Valley (up to 3.3×10^{16} molec cm^{-2}, 19 % error) and the Netherlands. The improved algorithm is also sensi-

tive above the UK (Sutton et al., 2013) and suggests marked emissions in eastern Europe.

The nighttime measurements show similar hotspots (bottom panel, Fig. 10), but with larger relative errors caused by the general lower thermal contrast for the nighttime overpass. On a daily basis, the morning and evening distributions can be quite different as the measurements will be strongly dependent on the local thermal contrast (in several places, morning and evening measurements bring complementary information). While nighttime measurements of NH$_3$ have been reported before (Clarisse et al., 2010), this is the first time that a global nighttime distribution is obtained, which constitutes in itself an important improvement over previous work.

Another major improvement compared to previous studies (both from IASI or TES) is the clear observation of large transported plumes NH$_3$, on the south coast of western Africa, around India and Mexico, and to lesser extent off the east coast of the United States. Atmospheric transport of NH$_3$ above the Mediterranean and Adriatic seas, emitted from agricultural activities in the Spanish Ebro and Italian Po valleys, respectively, is also observed by IASI as well as more sporadic transport events on the Plata River (Argentine coast). These results are spatially consistent with modeled distributions of Nr deposition (Duce et al., 2008) and with NH$_x$ wet deposition simulations (Dentener et al., 2006). A monthly distribution of NH$_3$ columns (February 2011) is depicted in Fig. 12, showing (1) transported fires plumes on the west and south coasts of western Africa, (2) NH$_3$ transported from agricultural sources on the west coast of India, (3) the Bay of Bengal, and (4) the Gulf of Guinea. The source types have been attributed by comparing the NH$_3$ distribution with fire radiative power (FRP) measurements from the MODerate resolution Imaging Spectroradiometer (MODIS) instrument (Justice et al., 2011). Similar export of NH$_3$ from biomass combustion and other continental sources to the ocean has already been reported for the Atlantic and Indian
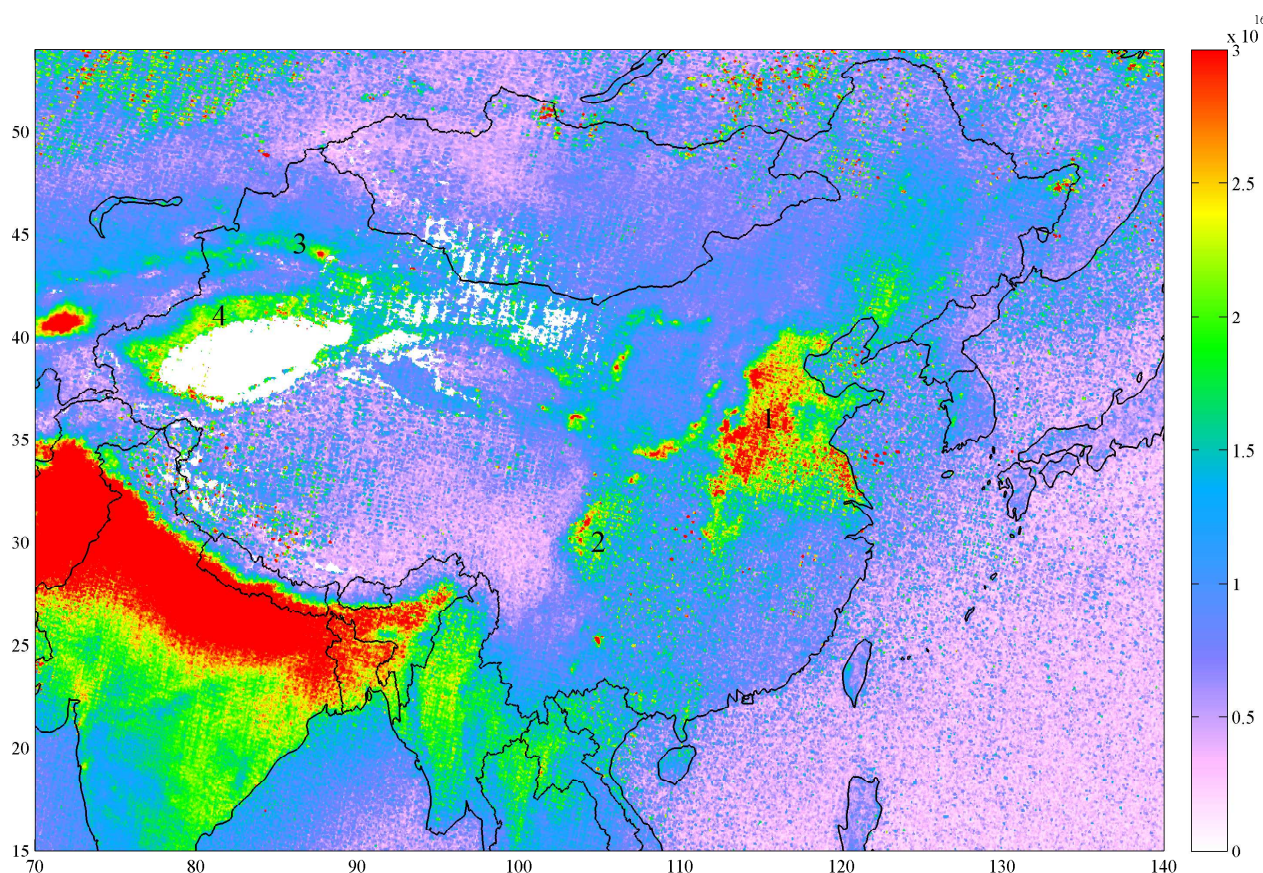
Fig. 13. NH$_3$ distribution over eastern Asia (molec cm^{-2}), following a griding method explicitly accounting for the IASI footprint on each individual measurement. The distribution is a five-year error-weighted average of the IASI daytime total columns in the region (a post-filtering excluding cells with less than 10 observations has been carried out over land).

oceans (Norman and Leck, 2005) and for the Bay of Bengal (Sharma et al., 2012) during ship campaigns.

The griding method used for the global distribution in Fig. 10 is not the most suitable for analyzing the NH$_3$ spatial distributions at smaller scales, as it smooths out some of the finer features. Figure 13 shows the regional NH$_3$ distribution over eastern Asia as an example, where each column is distributed in the corresponding IASI footprint (circular to ellipse-shaped, depending on the angle off nadir) before being averaged in a smaller 0.05° × 0.05° grid, following the same method as described above (i.e., error weighted averages, Eqs. 3 and 4). Fine-scale details of the emission regions are clearly revealed, with larger column values in areas where there is intensive agriculture. This is the case especially in the Hebei, Henan, Shandong and Jiangsu provinces (North China Plain, 1 in Fig. 13), which altogether account for approximately 30 % of the N fertilizer consumption and 33 % of the crop production in China in 2006 (Zhang et al., 2010; Huang et al., 2012). The North China Plain as a whole is responsible for 43 % of the NH$_3$ emitted from fertilization in China, while it represents only 3.3 % of the national area (Zhang et al., 2010; Huang et al., 2012). Several smaller

hotspots are detected in Fig. 13, including (2) the Sichuan province where the emissions are mainly from livestock, (3) the Xinjiang province, near Ürümqi and in Dzungaria and (4) around the Tarim basin, where there are sheep manure management and intensive fertilizer use (Huang et al., 2012; Li et al., 2012). Overall, the patterns observed above China are in excellent qualitative agreement with the distribution of sources from the recent emission inventory of Huang et al. (2012).

4.3 Temporal evolution

In Fig. 14 we show the first time series of daily retrieved NH$_3$ columns above land over the course of the five years averaged separately for the entire Northern (NH) and Southern Hemispheres (SH). The average values were calculated following Eq. (3), using only the columns measured during the morning orbits of IASI. Higher columns are measured in the Northern Hemisphere (on average for the five years 1.5×10^{16} molec cm^{-2}) as compared to the Southern Hemisphere (1.1×10^{16} molec cm^{-2}), which is mainly due
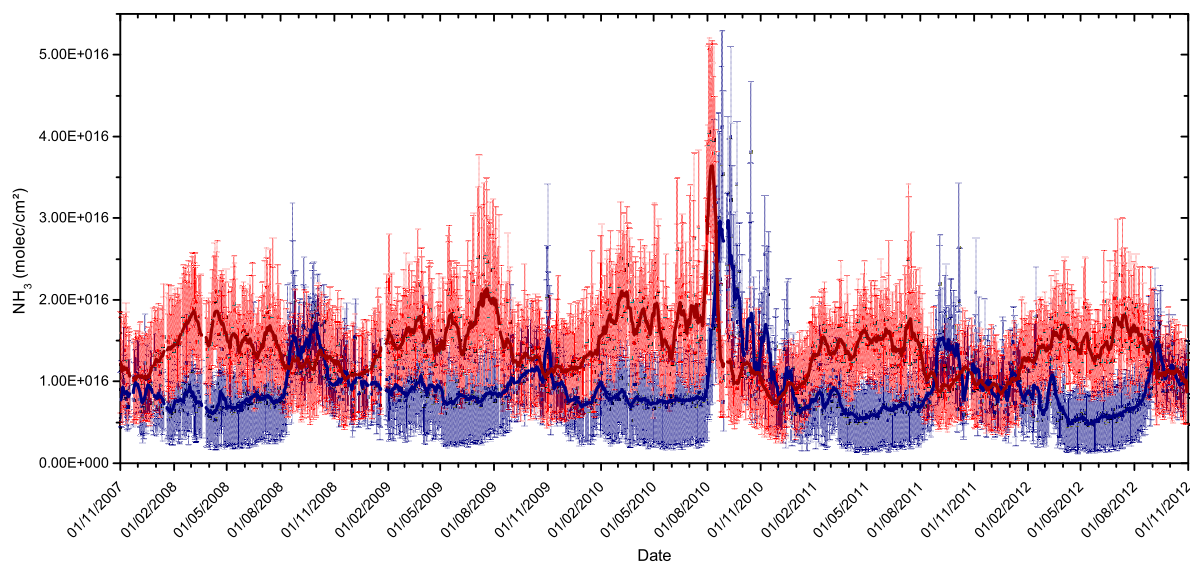
Fig. 14. Time series of daytime NH$_3$ total columns above land, averaged each day separately over the Northern (NH, red) and the Southern (SH, blue) Hemispheres. The error bars correspond to the error calculated as Eq. (4) around the daily mean value. The red and blue lines are 11 day running means.

to the dominance of agricultural sources in the northern part of the globe.

A seasonal cycle is observed in both hemispheres, with peak columns during local spring and summer. The seasonality in the Northern Hemisphere is especially pronounced, with columns varying from about 1×10^{16} molec cm^{-2} in winter (from October to February) up to double in spring and summer. The large columns measured throughout August 2010, which increase the average hemispheric column up to 4×10^{16} molec cm^{-2} on 5 August, are due to the large fires in central Russia (see, e.g., Figs. 6 and R'Honi et al., 2013). In the Southern Hemisphere the seasonal cycle is less marked, the maximum columns being typically observed there for a three-month period extending from August to October, which corresponds to the biomass burning period in South America and southern Africa. In 2010 the emission processes were particularly strong in South America and the average hemispheric NH$_3$ value reaches 4.1×10^{16} on 27 August. Note that the variations in the NH$_3$ columns as a function of the fire activity (from year to year) is qualitatively similar to that observed for carbon monoxide, for which large enhancements in 2010 in particular have been reported (Worden et al., 2013).

5   Conclusions and perspectives

We have described an improved method for the retrieval of NH$_3$ total column concentrations from IASI spectra, with improved sensitivity and near real-time applicability. The method follows a two-step process. The first step consists of measuring a so-called Hyperspectral Range Index from each

IASI spectrum using an optimal-estimation like approach, in which the measurement variance–covariance matrix is set to represent the total spectral variability that is not attributable to NH$_3$. A spectral range extending from 800 to 1200 cm^{-1}, larger than that used in previous studies, was selected and the matrix was built using one day of IASI measurements. In a second step the HRI is converted into a total column of NH$_3$, using look-up tables (separately for sea and land) built from forward radiative transfer calculations and considering a large number of different atmospheric conditions. The error on the retrieved total columns was estimated from the look-up tables and shown to be strongly related to the thermal contrast, varying from more than 100 % to lower than 25 % error for the most favorable situations. The latter are usually above land and during daytime, when there is a combination of high thermal contrast and enhanced NH$_3$. We show that this improved method retrieves NH$_3$ with improved sensitivity over previous retrieval schemes. A detailed comparison with the retrieval results from the FORLI software, which uses a full radiative transfer model, showed good agreement overall (correlation coefficient of 0.81, with FORLI biased high by 35 %).

Retrievals of the NH$_3$ columns for five years of IASI measurements have been performed, from which spatial distributions (separately for morning and evening orbits of IASI) and first time series have been derived and analyzed. A number of new hotspots have been identified from the five-year average global distributions, further highlighting the gain in sensitivity over earlier retrieval schemes. Export of NH$_3$, principally on the west coast of Africa and around India and Mexico, have been observed for the first time. We have shown with the

example of eastern Asia that the improved retrieval method also detects fine patterns of emissions on the regional scale. Seasonal cycles have been studied from the time series, separately for the Northern and Southern Hemispheres. The seasonality was shown to be more pronounced in the Northern Hemisphere, with peak columns in spring and summer. In the Southern Hemisphere, the seasonality is principally related to the biomass burning activity, which leads to column enhancements mainly from August to October. The summer 2010 stands out in the time series in both hemispheres as a result of the exceptional fires in Russia and in South America and Africa that year.

Currently both MetOp-A and MetOp-B are in operation and so in the near future twice as much data will be available. The IASI program is foreseen to last at least 15 years and will be followed up by the IASI-NG mission aboard the MetOp-SG satellite series (Clerbaux and Crevoisier, 2013). IASI will therefore provide the means to study global emissions of NH_3 and the long-term trends. Observation of NH_3 export may also provide new information to assess the ocean fertilization from atmospheric NH_3 deposition and the residence time of this trace gas in export plumes. The high spatial and temporal sampling of IASI observations also offers a suitable tool for evaluation of regional and global models. For these purposes, validation (which is ongoing) is required, which is challenging as both the infrared satellite measurements and other monitoring methods each have their own set of limitations. Nevertheless, the complementarities between ground-based, airborne, and ship measurements with satellite instruments and associated modeling efforts will increasingly enable better assessments of the local to global atmospheric NH_3 budget, spatial distributions, and long-term trends.

References

Adon, M., Galy-Lacaux, C., Yoboué, V., Delon, C., Lacaux, J. P., Castera, P., Gardrat, E., Pienaar, J., Al Ourabi, H., Laouali, D., Diop, B., Sigha-Nkamdjou, L., Akpo, A., Tathy, J. P., Lavenu, F., and Mougin, E.: Long term measurements of sulfur dioxide, nitrogen dioxide, ammonia, nitric acid and ozone in Africa using passive samplers, Atmos. Chem. Phys., 10, 7467–7487, doi:10.5194/acp-10-7467-2010, 2010.

August, T., Klaes, D., Schlüssel, P., Hultberg, T., Crapeau, M., Arriaga, A., O'Carroll, A., Coppens, D., Munro, R., and Calbet, X.: IASI on Metop-A: Operational Level 2 retrievals after five years in orbit, J. Quant. Spectrosc. Radiat. Transfer., 113, 1340–1371, doi:10.1016/j.jqsrt.2012.02.028, 2012.

Bauduin, S., Clarisse, L., Clerbaux, C., Hurtmans, D. and Coheur, P.-F.: IASI observations of sulfur dioxide (SO2) in the boundary layer of Norilsk, J. Geophys. Rese.-Atmos., doi:10.1002/2013JD021405, in press, 2014.

Beer, R., Shephard, M. W., Kulawik, S. S., Clough, S. A., Eldering, A., Bowman, K. W., Sander, S. P., Fisher, B. M., Payne, V. H., Luo, M., Osterman, G. B., and Worden, J. R.: First satellite observations of lower tropospheric ammonia and methanol, Geophys. Res. Lett., 35, L09801, doi:10.1029/2008GL033642, 2008.

Bobbink, R., Hicks, K., Galloway, J., Spranger, T., Alkemade, R., Ashmore, M., Bustamante, M., Cinderby, S., Davidson, E., Dentener, F., Emmett, B., Erisman, J.-W., Fenn, M., Gilliam, F., Nordin, A., Pardo, L., and De Vries, W.: Global assessment of nitrogen deposition effects on terrestrial plant diversity: a synthesis, Ecol. Appl., 20, 30–59, doi:10.1890/08-1140.1, 2010.

Chevallier, F.: Sampled databases of 60-level atmospheric profiles from the ECMWF analyses, Research Report 4, Eumetsat/ECMWF SAF Programme, 2001.

Clarisse, L., Clerbaux, C., Dentener, F., Hurtmans, D., and Coheur, P.-F.: Global ammonia distribution derived from infrared satellite observations, Nat. Geosci., 2, 479–483, doi:10.1038/ngeo551, 2009.

Clarisse, L., Shephard, M., Dentener, F., Hurtmans, D., Cady-Pereira, K., Karagulian, F., Van Damme, M., Clerbaux, C., and Coheur, P.-F.: Satellite monitoring of ammonia: A case study of the San Joaquin Valley, J. Geophys. Res., 115, D13302, doi:10.1029/2009JD013291, 2010.

Clarisse, L., R'Honi, Y., Coheur, P.-F., Hurtmans, D., and Clerbaux, C.: Thermal infrared nadir observations of 24 atmospheric gases, Geophys. Res. Lett., 38, L10802, doi:10.1029/2011GL047271, 2011.

Clarisse, L., Coheur, P.-F., Prata, F., Hadji-Lazaro, J., Hurtmans, D., and Clerbaux, C.: A unified approach to infrared aerosol remote sensing and type specification, Atmos. Chem. Phys., 13, 2195–2221, doi:10.5194/acp-13-2195-2013, 2013.

Clerbaux, C., Boynard, A., Clarisse, L., George, M., Hadji-Lazaro, J., Herbin, H., Hurtmans, D., Pommier, M., Razavi, A., Turquety, S., Wespes, C., and Coheur, P.-F.: Monitoring of atmospheric composition using the thermal infrared IASI/MetOp sounder, Atmos. Chem. Phys., 9, 6041–6054, doi:10.5194/acp-9-6041-2009, 2009.

Coheur, P.-F., Barret, B., Turquety, S., Hurtmans, D., Hadji-Lazaro, J., and Clerbaux, C.: Retrieval and characterization of ozone vertical profiles from a thermal infrared nadir sounder, J. Geophys. Res.-Atmos., 110, D24303, doi:10.1029/2005JD005845, 2005.

Coheur, P.-F., Clarisse, L., Turquety, S., Hurtmans, D., and Clerbaux, C.: IASI measurements of reactive trace species in biomass burning plumes, Atmos. Chem. Phys., 9, 5655–5667, doi:10.5194/acp-9-5655-2009, 2009.

Deeter, M. N., Edwards, D. P., Gille, J. C., and Drummond, J. R.: Sensitivity of MOPITT observations to carbon monoxide in the lower troposphere, J. Geophys. Res.-Atmos., 112, D24306, doi:10.1029/2007JD008929, 2007.

Dentener, F., Drevet, J., Lamarque, J. F., Bey, I., Eickhout, B., Fiore, A. M., Hauglustaine, D., Horowitz, L. W., Krol, M., Kulshrestha, U. C., Lawrence, M., Galy-Lacaux, C., Rast, S., Shindell, D., Stevenson, D., Van Noije, T., Atherton, C., Bell, N., Bergman, D., Butler, T., Cofala, J., Collins, B., Doherty, R., Ellingsen, K., Galloway, J., Gauss, M., Montanaro, V., Müller, J. F., Pitari, G., Rodriguez, J., Sanderson, M., Solmon, F., Strahan, S., Schultz, M., Sudo, K., Szopa, S., and Wild, O.: Nitrogen and sulfur deposition on regional and global scales: A multimodel evaluation, Global Biogeochem. Cy., 20, GB4003, doi:10.1029/2005GB002672, 2006.

Diaz, R. J. and Rosenberg, R.: Introduction to Environmental and Economic Consequences of Hypoxia, Int. J. Water Resour. D., 27, 71–82, doi:10.1080/07900627.2010.531379, 2011.

Duce, R. A., LaRoche, J., Altieri, K., Arrigo, K. R., Baker, A. R., Capone, D. G., Cornell, S., Dentener, F., Galloway, J., Ganeshram, R. S., Geider, R. J., Jickells, T., Kuypers, M. M., Langlois, R., Liss, P. S., Liu, S. M., Middelburg, J. J., Moore, C. M., Nickovic, S., Oschlies, A., Pedersen, T., Prospero, J., Schlitzer, R., Seitzinger, S., Sorensen, L. L., Uematsu, M., Ulloa, O., Voss, M., Ward, B., and Zamora, L.: Impacts of Atmospheric Anthropogenic Nitrogen on the Open Ocean, Science, 320, 893–897, doi:10.1126/science.1150369, 2008.

EDGAR-Emission Database for Global Atmospheric Research: Results of the emission inventory EDGAR v4.1 of July 2010, available at: http://edgar.jrc.ec.europa.eu (last access: 13 July 2013), 2010.

EDGAR-Emission Database for Global Atmospheric Research: Source: EC-JRC/PBL. EDGAR version 4.2., available at: http://edgar.jrc.ec.europa.eu (last access: 15 October 2012), 2011.

EEA-European Environment Agency: Ammonia (NH3) emissions (APE 003), Assessment published December 2012, last access: 15 July 2013, 2012.

Environment Canada: National Pollutant Release Inventory, available at: http://www.ec.gc.ca/inrp-npri/default.asp?lang=En&n=E788969F-1 (last access: 19 July 2013), 2013.

Erisman, J. W. and Schaap, M.: The need for ammonia abatement with respect to secondary PM reductions in Europe, Environ. Pollut., 129, 159–163, doi:10.1016/j.envpol.2003.08.042, 2004.

Erisman, J. W., Grennfelt, P., and Sutton, M.: The European perspective on nitrogen emission and deposition, Environ. Int., 29, 311–325, doi:10.1016/S0160-4120(02)00162-9, 2003.

Erisman, J. W., Bleeker, A., Galloway, J., and Sutton, M.: Reduced nitrogen in ecology and the environment, Environ. Pollut., 150, 140–149, doi:10.1016/j.envpol.2007.06.033, 2007.

Erisman, J. W., Galloway, J. N., Seitzinger, S., Bleeker, A., Dise, N. B., Petrescu, A. M. R., Leach, A. M., and de Vries, W.: Consequences of human modification of the global nitrogen cycle, Philos. Trans. R. Soc. London, Ser. B, 368, 1621, doi:10.1098/rstb.2013.0116, 2013.

Fowler, D., Coyle, M., Skiba, U., Sutton, M. A., Cape, J. N., Reis, S., Sheppard, L. J., Jenkins, A., Grizzetti, B., Galloway, J. N., Vitousek, P., Leach, A., Bouwman, A. F., Butterbach-Bahl, K., Dentener, F., Stevenson, D., Amann, M., and Voss, M.: The global nitrogen cycle in the twenty-first century, Philos. Trans. R. Soc. London, Ser. B, 368, 2621, doi:10.1098/rstb.2013.0164, 2013.

Galloway, J., Aber, J., Erisman, J., Seitzinger, S., Howarth, R., Cowling, E., and Cosby, B.: The Nitrogen Cascade, BioScience, 53, 341–356, 2003.

Galloway, J. N., Townsend, A. R., Erisman, J. W., Bekunda, M., Cai, Z., Freney, J. R., Martinelli, L. A., Seitzinger, S. P., and Sutton, M. A.: Transformation of the Nitrogen Cycle: Recent Trends, Questions, and Potential Solutions, Science, 320, 889–892, doi:10.1126/science.1136674, 2008.

Ginoux, P., Clarisse, L., Clerbaux, C., Coheur, P.-F., Dubovik, O., Hsu, N. C., and Van Damme, M.: Mixing of dust and NH₃ observed globally over anthropogenic dust sources, Atmos. Chem. Phys., 12, 7351–7363, doi:10.5194/acp-12-7351-2012, 2012.

Heald, C. L., Jr., J. L. C., Lee, T., Benedict, K. B., Schwandner, F. M., Li, Y., Clarisse, L., Hurtmans, D. R., Van Damme, M., Clerbaux, C., Coheur, P.-F., Philip, S., Martin, R. V., and Pye, H. O. T.: Atmospheric ammonia and particulate inorganic nitrogen over the United States, Atmos. Chem. Phys., 12, 10295–10312, doi:10.5194/acp-12-10295-2012, 2012.

Hilton, F., Armante, R., August, T., Barnet, C., Bouchard, A., Camy-Peyret, C., Capelle, V., Clarisse, L., Clerbaux, C., Coheur, P.-F., Collard, A., Crevoisier, C., Dufour, G., Edwards, D., Faijan, F., Fourrié, N., Gambacorta, A., Goldberg, M., Guidard, V., Hurtmans, D., Illingworth, S., Jacquinet-Husson, N., Kerzenmacher, T., Klaes, D., Lavanant, L., Masiello, G., Matricardi, M., McNally, A., Newman, S., Pavelin, E., Payan, S., Péquignot, E., Peyridieu, S., Phulpin, T., Remedios, J., Schlüssel, P., Serio, C., Strow, L., Stubenrauch, C., Taylor, J., Tobin, D., Wolf, W., and Zhou, D.: Hyperspectral Earth Observation from IASI: Five Years of Accomplishments, Bull. Am. Meteorol. Soc., 93, 347–370, doi:10.1175/BAMS-D-11-00027.1, 2012.

Huang, X., Song, Y., Li, M., Li, J., Huo, Q., Cai, X., Zhu, T., Hu, M., and Zhang, H.: A high-resolution ammonia emission inventory in China, Global Biogeochem. Cy., 26, GB1030, doi:10.1029/2011GB004161, 2012.

Hurtmans, D., Coheur, P.-F., Wespes, C., Clarisse, L., Scharf, O., Clerbaux, C., Hadji-Lazaro, J., George, M., and Turquety, S.: FORLI radiative transfer and retrieval code for IASI, J. Quant. Spectrosc. Radiat. Transfer., 1391–1408, doi:10.1016/j.jqsrt.2012.02.036, 2012.

Justice, C. O., Giglio, L., Roy, D., Boschetti, L., Csiszar, I., Davies, D., Korontzi, S., Schroeder, W., O'Neal, K., and Morisette, J.: MODIS-Derived Global Fire Products, in: Land Remote Sensing and Global Environmental Change, edited by: Ramachandran, B., Justice, C. O., and Abrams, M. J., Vol. 11 of Remote Sensing and Digital Image Processing, 661–679, Springer New York, doi:10.1007/978-1-4419-6749-7_29, 2011.

Kharol, S. K., Martin, R. V., Philip, S., Vogel, S., Henze, D. K., Chen, D., Wang, Y., Zhang, Q., and Heald, C. L.: Persistent sensitivity of Asian aerosol to emissions of nitrogen oxides, Geophys. Res. Lett., 40, 1021–1026, doi:10.1002/grl.50234, 2013.

Krupa, S.: Effects of atmospheric ammonia (NH$_3$) on terrestrial vegetation: a review, Environ. Pollut., 124, 179–221, doi:10.1016/S0269-7491(02)00434-7, 2003.

LADA: Mapping Land Use Systems and global and regional scale for Land Degradation Assessment Analysis, LADA technical report 8, Vol. 1.1, edited by: Nachtergaele, F. and Petri, M., 2008.

Laj, P., Klausen, J., Bilde, M., Plaß-Duelmer, C., Pappalardo, G., Clerbaux, C., Baltensperger, U., Hjorth, J., Simpson, D., Reimann, S., Coheur, P.-F., Richter, A., Mazière, M. D., Rudich, Y., McFiggans, G., Torseth, K., Wiedensohler, A., Morin, S., Schulz, M., Allan, J., Attié, J.-L., Barnes, I., Birmili, W., Cammas, J., Dommen, J., Dorn, H.-P., Fowler, D., Fuzzi, S., Glasius, M., Granier, C., Hermann, M., Isaksen, I., Kinne, S., Koren, I., Madonna, F., Maione, M., Massling, A., Moehler, O., Mona, L., Monks, P., Müller, D., Müller, T., Orphal, J., Peuch, V.-H., Stratmann, F., Tanré, D., Tyndall, G., Riziq, A. A., Van Roozendael, M., Villani, P., Wehner, B., Wex, H., and Zardini, A.: Measuring atmospheric composition change, Atmos. Environ., 43, 5351–5414, doi:10.1016/j.atmosenv.2009.08.020, 2009.

Li, K. H., Song, W., Liu, X. J., Shen, J. L., Luo, X. S., Sui, X. Q., Liu, B., Hu, Y. K., Christie, P., and Tian, C. Y.: Atmospheric reactive nitrogen concentrations at ten sites with contrasting land use in an arid region of central Asia, Biogeosciences, 9, 4013–4021, doi:10.5194/bg-9-4013-2012, 2012.

NASA: Crop Circles in the Desert, available at: http://earthobservatory.nasa.gov/IOTD/view.php?id=77900 (last access: 15 December 2012), landsat 5 – TM images, 2012.

Norman, M. and Leck, C.: Distribution of marine boundary layer ammonia over the Atlantic and Indian Oceans during the Aerosols99 cruise, J. Geophys. Res.-Atmos., 110, D16302, doi:10.1029/2005JD005866, 2005.

Nowak, J. B., Neuman, J. A., Kozai, K., Huey, L. G., Tanner, D. J., Holloway, J. S., Ryerson, T. B., Frost, G. J., McKeen, S. A., and Fehsenfeld, F. C.: A chemical ionization mass spectrometry technique for airborne measurements of ammonia, J. Geophys. Res.-Atmos., 112, D10S02, doi:10.1029/2006JD007589, 2007.

Nowak, J. B., Neuman, J. A., Bahreini, R., Brock, C. A., Middlebrook, A. M., Wollny, A. G., Holloway, J. S., Peischl, J., Ryerson, T. B., and Fehsenfeld, F. C.: Airborne observations of ammonia and ammonium nitrate formation over Houston, Texas, J. Geophys. Res.-Atmos., 115, D22304, doi:10.1029/2010JD014195, 2010.

Pinder, R. W., Gilliland, A. B., and Dennis, R. L.: Environmental impact of atmospheric NH$_3$ emissions under present and future conditions in the eastern United States, Geophys. Res. Lett., 35, L12808, doi:10.1029/2008GL033732, 2008.

Potter, P., Ramankutty, N., Bennett, E. M., and Donner, S. D.: Characterizing the Spatial Patterns of Global Fertilizer Application and Manure Production, Earth Interact., 14, 1–22, doi:10.1175/2009EI288.1, 2010.

Pougatchev, N., August, T., Calbet, X., Hultberg, T., Oduleye, O., Schlüssel, P., Stiller, B., Germain, K. S., and Bingham, G.: IASI temperature and water vapor retrievals - error assessment and validation, Atmos. Chem. Phys., 9, 6453–6458, doi:10.5194/acp-9-6453-2009, 2009.

Reis, S., Pinder, R. W., Zhang, M., Lijie, G., and Sutton, M. A.: Reactive nitrogen in atmospheric emission inventories, Atmos. Chem. Phys., 9, 7657–7677, doi:10.5194/acp-9-7657-2009, 2009.

R'Honi, Y., Clarisse, L., Clerbaux, C., Hurtmans, D., Duflot, V., Turquety, S., Ngadi, Y., and Coheur, P.-F.: Exceptional emissions of NH$_3$ and HCOOH in the 2010 Russian wildfires, Atmos. Chem. Phys., 13, 4171–4181, doi:10.5194/acp-13-4171-2013, 2013.

Rockström, J., Steffen, W., Noone, K., Persson, A., Chapin, F. S., Lambin, E. F., Lenton, T. M., Scheffer, M., Folke, C., Schellnhuber, H. J., Nykvist, B., de Wit, C. A., Hughes, T., van der Leeuw, S., Rodhe, H., Sorlin, S., Snyder, P. K., Costanza, R., Svedin, U., Falkenmark, M., Karlberg, L., Corell, R. W., Fabry, V. J., Hansen, J., Walker, B., Liverman, D., Richardson, K., Crutzen, P., and Foley, J. A.: A safe operating space for humanity, Nature, 461, 472–475, doi:10.1038/461472a, 2009.

Rodgers, C.: Inverse Methods for Atmospheric Sounding: Theory and Practice, World Scientific, 2000.

Scheer, C., Wassmann, R., Kienzler, K., Ibragimov, N., and Eschanov, R.: Nitrous oxide emissions from fertilized, irrigated cotton (<textslGossypium hirsutum L.) in the Aral Sea Basin, Uzbekistan: Influence of nitrogen applications and irrigation practices, Soil Biol. Biochem., 40, 290–301, doi:10.1016/j.soilbio.2007.08.007, 2008.

Seinfeld, J.: Atmospheric chemistry and physics of air pollution, Wiley, 738 pp., 1986.

Sharma, S. K., Singh, A. K., Saud, T., Mandal, T. K., Saxena, M., Singh, S., Ghosh, S. K., and Raha, S.: Measurement of ambient NH$_3$ over Bay of Bengal during W_ICARB Campaign, Ann. Geophys., 30, 371–377, doi:10.5194/angeo-30-371-2012, 2012.

Shephard, M. W., Cady-Pereira, K. E., Luo, M., Henze, D. K., Pinder, R. W., Walker, J. T., Rinsland, C. P., Bash, J. O., Zhu, L., Payne, V. H., and Clarisse, L.: TES ammonia retrieval strategy and global observations of the spatial and seasonal variability of ammonia, Atmos. Chem. Phys., 11, 10743–10763, doi:10.5194/acp-11-10743-2011, 2011.

Sutton, M. A., Oenema, O., Erisman, J. W., Leip, A., van Grinsven, H., and Winiwarter, W.: Too much of a good thing, Nature, 472, 159–161, doi:10.1038/472159a, 2011.

Sutton, M. A., Reis, S., Riddick, S. N., Dragosits, U., Nemitz, E., Theobald, M. R., Tang, Y. S., Braban, C. F., Vieno, M., Dore, A. J., Mitchell, R. F., Wanless, S., Daunt, F., Fowler, D., Blackall, T. D., Milford, C., Flechard, C. R., Loubet, B., Massad, R., Cellier, P., Personne, E., Coheur, P. F., Clarisse, L., Van Damme, M., Ngadi, Y., Clerbaux, C., Skjth, C. A., Geels, C., Hertel, O., Wichink Kruit, R. J., Pinder, R. W., Bash, J. O., Walker, J. T., Simpson, D., Horvth, L., Misselbrook, T. H., Bleeker, A., Dentener, F., and de Vries, W.: Towards a climate-dependent paradigm of ammonia emission and deposition, Philos. Trans. R. Soc. London, Ser. B, 368, doi:10.1098/rstb.2013.0166, 2013.

Walker, J. C., Dudhia, A., and Carboni, E.: An effective method for the detection of trace species demonstrated using the MetOp Infrared Atmospheric Sounding Interferometer, Atm. Meas. Tech., 4, 1567–1580, doi:10.5194/amt-4-1567-2011, 2011.

Walker, J. M., Philip, S., Martin, R. V., and Seinfeld, J. H.: Simulation of nitrate, sulfate, and ammonium aerosols over the United States, Atmos. Chem. Phys., 12, 11213–11227, doi:10.5194/acp-12-11213-2012, 2012.

Worden, H. M., Deeter, M. N., Frankenberg, C., George, M., Nichitiu, F., Worden, J., Aben, I., Bowman, K. W., Clerbaux, C., Coheur, P. F., de Laat, A. T. J., Detweiler, R., Drummond, J. R., Edwards, D. P., Gille, J. C., Hurtmans, D., Luo, M., Martínez-Alonso, S., Massie, S., Pfister, G., and Warner, J. X.: Decadal record of satellite carbon monoxide observations, Atmos. Chem. Phys., 13, 837–850, doi:10.5194/acp-13-837-2013, 2013.

Zhang, Y., Dore, A., Ma, L., Liu, X., Ma, W., Cape, J., and Zhang, F.: Agricultural ammonia emissions inventory and spatial distribution in the North China Plain, Environ. Pollut., 158, 490 – 501, doi:10.1016/j.envpol.2009.08.033, 2010.

Zhou, D., Larar, A., Liu, X., Smith, W., Strow, L., Yang, P., Schlussel, P., and Calbet, X.: Global Land Surface Emissivity Retrieved From Satellite Ultraspectral IR Measurements, IEEE T. Geosci. Remote, 49, 1277–1290, doi:10.1109/TGRS.2010.2051036, 2011.

Zhu, L., Henze, D. K., Cady-Pereira, K. E., Shephard, M. W., Luo, M., Pinder, R. W., Bash, J. O., and Jeong, G.-R.: Constraining U.S. ammonia emissions using TES remote sensing observations and the GEOS-Chem adjoint model, J. Geophys. Res.-Atmos., 118, 3355–3368, doi:10.1002/jgrd.50166, 2013.